WWF
Last Ice Area

Technical report

DAVID HUARD, PhD

BRUNO TREMBLAY, PhD

McGill

DavidHuard
SOLUTIONS
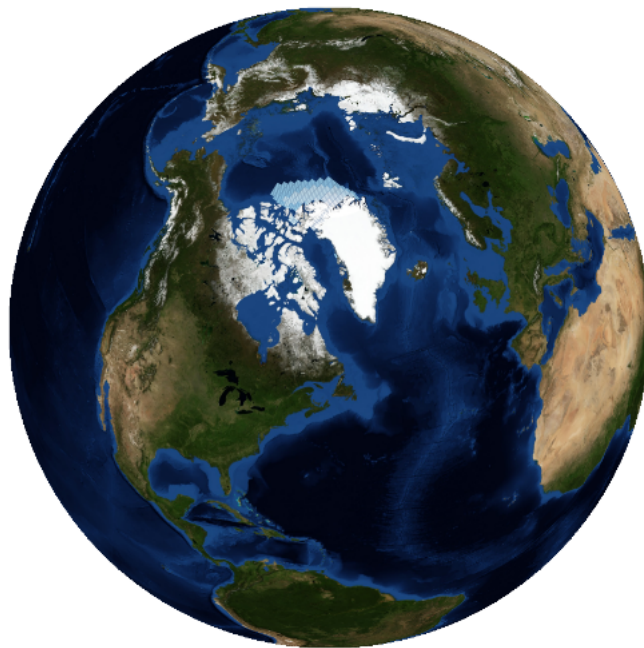
WWF Last Ice Area

Authors :   David Huard, Bruno Tremblay

Abstract

The purpose of this project is to illustrate the fate of Arctic sea ice over the next decades. Part A of the project looks at results from an ensemble of global climate model projections. The objective of Part A is to explore the various pathways of future ice loss as simulated by different climate models driven by two radiative forcing scenarios. The impact of climate change on Arctic conditions is diagnosed through sea ice concentration, sea ice thickness and snow depth over ice. Part B completes the picture by running a high-resolution (18km) regional ocean and ice model, providing finer spatial details of ice conditions projected by the GFDL Climate Model version 3 under the business-as-usual RCP8.5 forcing scenario.

February 15, 2013

Contents

List of Figures

List of Tables

Introduction

Anthropogenic emissions of greenhouse gases and aerosols (GHGA) over the past hundreds years have modified the chemical composition of the atmosphere. This modification is affecting the radiative properties of the atmosphere: due to greenhouse gasess (GHGs), the atmosphere is now more opaque to space-bound infrared radiation from the Earth. Infrared, or long-wave, radiation is the only process by which the Earth can shed the heat it receives from the Sun. The outgoing longwave radiation emitted from the Earth to space being less then the incoming solar radiation because of increased GHGs concentration, the Earth is accumulating energy and warming.

At face value, the effect of this increase in GHG on the radiative balance is relatively weak compared to seasonal variations in radiation. In 2005, carbon dioxide (CO_2) was estimated to contribute 1.66 W/m² of radiative forcing [*Forster et al.*, 2007], a small amount compared to the 250 W/m² received on an average day. The impact is now noticeable because this small imbalance accumulates, and the response of the system is amplified by positive feedbacks. The main positive feedback is called the water vapour feedback. At higher temperatures, more water vapour remains in gas form before it condenses and falls as precipitation. As CO_2, water vapor is a GHG that absorbs infrared radiation emitted by the Earth and keeps the surface warmer than it would be in the its absence. This water-vapour feedback roughly doubles the effect of the anthropogenic CO_2 alone [*Held and Soden*, 2000].

Another important feedback is the ice albedo feedback. The albedo is a measure of the reflexivity of a surface. A white surface has a high albedo while a black or transparent surface has a low albedo since most of the light it receives is absorbed and converted into heat. On a scale from zero to one, sea ice in the Arctic has an albedo of about 0.7. In contrast, open water has an albedo of around 0.06. Given a slight increase in temperatures, more sea ice melts, increasing the area covered by open water. The net effect is the reduction of the surface albedo, thus a decrease in the amount of light that is reflected back to space. The surface thus absorbs more solar energy which leads to further warming and more sea ice melt.

Other feedback processes, some positive other negatives, reinforce or reduce the effects of GHGA. To understand how all these complex feedbacks interact with each

other, climatologists develop and use Global Coupled Models (GCMs). GCMs are simplified numerical representations of the main components of the Earth climate system. They solve the equations of fluid dynamics (movements of air and water), encode thermodynamic processes (temperature and phase changes) and compute the radiative properties of the atmosphere according to its composition (water vapour, CO_2, methane, chlorofluorocarbons, etc). Using powerful computers, these models simulate the climate to understand how it has changed in the past (paleo-climate) and what are plausible pathways for the future.

Models are only simplified representations of nature and cannot be expected to reproduce exactly its behaviour. This is even more true for climate models since climate is understood as a chaotic system. Chaotic means that even with a perfect model, slight perturbations in the initial conditions grow exponentially as time progresses. For this reason, we cannot expect to correctly simulate the weather at a particular time in the future, but rather the hope is to correctly simulate the mean weather (or climate) which is regulated by more predictable forcing such as solar insolation and GHGA. That is, we do not expect the events simulated by climate models to match the events occurring in the real world. What climate models do predict are the mean properties of the climate over long time scales. In practice, the World Meteorological Organization suggests a 30-year average to define the climate.

The interpretation of climate results is hence only meaningful when look at the general properties of the system, and not the individual events. One way climatologists do this is by analysing ensembles of simulations. A very revealing example is an initial conditions ensemble: a set of simulations run by the same climate model where the only differences between simulations are small variations in the initial conditions. Figure 1.1 shows the global mean temperature from an ensemble of 40 runs using the Community Climate System Model version 4 (CCSM4), where each simulation is started with initial conditions taken at random from a previous simulation [*Deser et al.*, 2010]. It is clear that, even by averaging over the entire globe, the interannual variations from the 40 simulations are completely independent. What does stand out is the steady increase in temperature and the spread around the mean. For climatologists, the trend is considered a robust climate change signal, while the yearly variations are merely noise. The spread around the mean is due to the chaotic nature of the climate system and is referred to as natural climatic variability.

The next section presents Arctic sea ice conditions from an ensemble of GCM simulations prepared for the Coupled Model Intercomparison Project Phase 5 (CMIP5). As shown in the last figure, short term variations from only one simulation are not meaningful. However, reliable information can be extracted either from long term averages or ensembles of many short-term simulations. The spatial resolution of most GCMs being rather coarse, on the order of 100km, fine scale details of sea ice conditions are lost and the second part of the project (part B) presents results from a high-resolution (18km) regional model of the Arctic, forced by atmospheric fields from a single member from one GCM. Again, this does not constitute a prediction of ice conditions, but simply a more detailed picture of one plausible future among
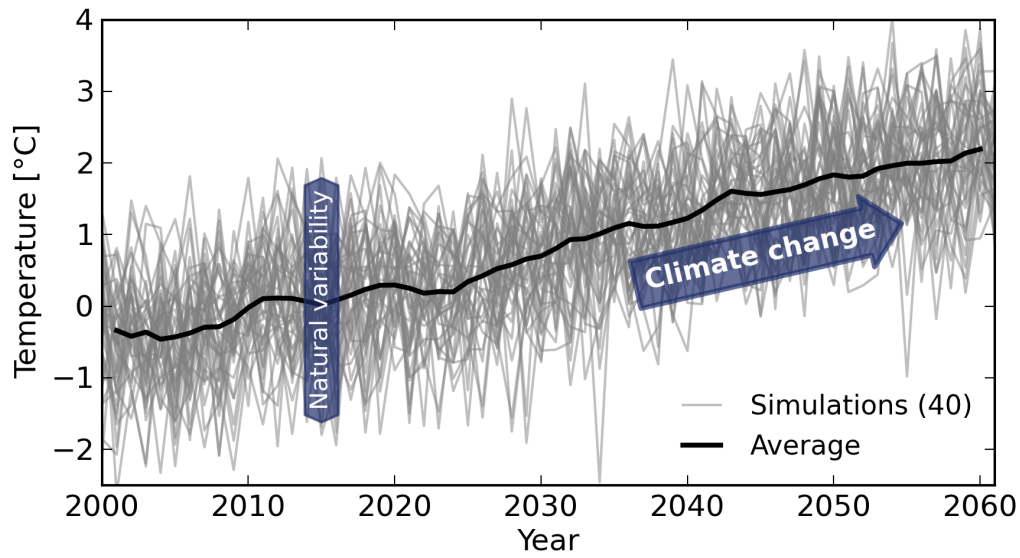
Figure 1.1: Annual global mean temperatures from 40 simulations of the CCSM4 Large Ensemble Experiment. The only difference between those simulations are small differences in initial conditions.

many. For this reason, we place more confidence in the spatial pattern of the sea ice retreat than in its actual timing.

Part A: Sea ice conditions from the CMIP5 ensemble

The work presented in this section paints a general picture of expected Arctic sea ice conditions from 1970 to 2100. Different models yield different answers, and the best way known to date to assign confidence to model outputs is to compare results from different models and identify robust features among them. Although there are other sources of uncertainty in climate modelling, such as the GHG emission scenario or natural variability, the choice of GCM is the leading one around the 2050 time frame [*Hawkins and Sutton*, 2009].

CMIP5 is an ongoing effort to compare simulations from climate modelling teams around the world [*Taylor et al.*, 2011]. To participate, each team is required to submit simulations following guidelines defined by the World Climate Research Programme's (WCRP) Working Group on Coupled Modelling (WGCM). These simulations are stored in each institution and distributed through the Earth System Grid (ESG) web portal federation. Simulations for this project were downloaded from ESG in October 2012. Simulations that have been made available since are hence not included in this report.

Among the experiments that modelling teams are required to run, three are of interest for this work: Historical, RCP4.5 and RCP8.5. Historical simulations are those driven by GHGA conditions as measured during the 20th century. RCP experiments stand for Radiative Concentration Pathways [*Moss et al.*, 2010] and describe radiative forcing scenarios over the period 2006–2300. While CMIP3 used emission scenarios based on plausible socioeconomic futures (A2, A1B or B1), CMIP5 skips the socioeconomic analysis step and proposes a range of plausible radiative forcings. RCP4.5 is a mid-range scenario where the globally averaged anthropogenic GHGA radiative forcing stabilizes in 2070 at about 4.5 W/m². RCP8.5 is the high-range, business as usual scenario where the globally averaged radiative forcing reaches 8.5 W/m² in 2100 and continues to rise afterwards.

2.1   Sea ice diagnostics

To build a comprehensive picture of the sea ice retreat and its potential impacts, WWF is interested in the fate of sea ice concentration but also sea ice thickness and snow depth. Table 2.1 lists all the models that were analyzed for this study for which sea ice concentration, sea ice thickness or snow depth over sea ice were available for the Historical, RCP4.5 and RCP8.5 experiments. The spatial resolution of different GCMs shows considerable variations, going from coarse (2.5° × 2.0°) to fine (0.45° × 0.39°).

2.2   Climatological mean maps

Model outputs from CMIP5 experiments are available at different temporal frequencies, from 3-hourly to monthly averages. In this project, monthly mean diagnostics were used for part A. Once data acquisition from the ESG portal was complete, model outputs were processed to compute monthly averages over longer time scales. Simulations from the Historical experiment were averaged over the 1970–1999 period, while RCP4.5 and RCP8.5 simulations were averaged over decades spanning the 21st century: 2000–2009, 2010–2019, ..., 2090–2099. Note that since RCP experiments are started in 2006, the 2000-2009 average only include years from 2006 to 2009. All these averages are saved in individual netCDF files.

    As per the project requirements, we converted these monthly averages into KMZ files. To this end, we followed the approach used by the National Snow & Ice Data Center (NSIDC) to distribute sea ice extent maps for GoogleEarth. Maps of sea ice extents are saved on a regular cylindrical projection then loaded as image overlays in KML documents. The most work intensive step has been to convert irregular model grids unto a cylindrical projection. Conversion from geographic coordinates to cylindrical coordinates is handled by mapping software, but handling grid cells wrapping around the pole or spanning the meridian boundary needed special care to avoid having blank spaces in the final post-processed maps. Figure 2.2 provides an examples of these blanks.

    Once the grid cells have been mapped onto the cylindrical projection, each cell value is color-coded using a colormap spanning the [0,95] percentile range. The 95% cut-off is used to avoid stretching the colormap over outlier values. This cut-off is computed for the historical period for the months of April and September. The same cutoffs were used as well for the other experiments (RCP4.5 and RCP8.5) and all decadal averages. Colormap examples for the CCSM4 model are shown in figure 2.1. Note that sea ice concentration values under 15% are transparent to provide a realistic looking sea ice edge. The 15% cut-off for the ice edge follows the criteria used at NSIDC. All KMZ[1] and netCDF files were provided to WWF as deliverable under the

---

[1]In the KML file, each image is associated with a `<TimeSpan>` tag spanning the averaging period. This means that the historical average covers the 1970–1999 period, and each decadal image spans 10 years over the 21st century. For some models, a land-mask contour has been added to the KML file to indicate ocean boundaries.

Table 2.1: Models for which sea ice concentration (SIC), sea ice thickness (SIT) or snow depth over sea ice (SND) were available in October 2012 for Historical, RCP4.5 and RCP8.5 experiments. Model horizontal resolutions are approximations in the case of irregular grids.

Model	Institute	Resolution	Available variables
ACCESS1-3	CSIRO and BOM, Australia	1.0° × 0.44°	SIC
BNU-ESM	GCESS, China	1.0° × 0.96°	SIC,SND
CCSM4	NCAR, U.S.A.	1.1° × 0.43°	SIC,SND,SIT
CESM1-CAM5	NSF-DOE-NCAR, U.S.A.	1.1° × 0.43°	SIC,SND,SIT
CMCC-CM	CMCC, Italy	2.0° × 1.0°	SIC
CMCC-CMS	CMCC, Italy	2.0° × 1.0°	SIC
CNRM-CM5	CNRM-CERFACS, France	1.0° × 0.48°	SIC,SIT
CanESM2	CCCma, Canada	2.8° × 2.8°	SIC,SND,SIT
EC-EARTH	EC-EARTH Consortium	1.0° × 0.48°	SIC
FGOALS-s2	LASG-IAP, China	1.0° × 1.0°	SIC,SND
GFDL-CM3	NOAA-GFDL, U.S.A.	1.0° × 0.96°	SIC,SND,SIT
GFDL-ESM2G	NOAA-GFDL, U.S.A.	1.0° × 0.88°	SIC,SND,SIT
GFDL-ESM2M	NOAA-GFDL, U.S.A.	1.0° × 0.96°	SIC,SND,SIT
GISS-E2-H	NASA-GISS, U.S.A.	2.5° × 2.0°	SIC
GISS-E2-R	NASA-GISS, U.S.A.	2.5° × 2.0°	SIC
HadGEM2-AO	MOHC, U.K.	1.0° × 1.0°	SIC,SIT
HadGEM2-CC	MOHC, U.K.	1.0° × 1.0°	SIC,SND,SIT
HadGEM2-ES	MOHC, U.K.	1.0° × 1.0°	SIC,SND,SIT
IPSL-CM5A-LR	IPSL, France	2.0° × 1.0°	SIC
IPSL-CM5A-MR	IPSL, France	2.0° × 1.0°	SIC
IPSL-CM5B-LR	IPSL, France	2.0° × 1.0°	SIC
MIROC-ESM	JAMSTEC-AORI-NIES, Japan	1.4° × 0.93°	SIC,SND,SIT
MIROC-ESM-CHEM	JAMSTEC-AORI-NIES, Japan	1.4° × 0.93°	SIC,SND,SIT
MIROC5	AORI-NIES-JAMSTEC, Japan	1.2° × 0.64°	SIC,SND,SIT
MPI-ESM-LR	MPI-M, Germany	1.2° × 0.64°	SIT
MPI-ESM-MR	MPI-M, Germany	0.45° × 0.39°	SIC,SIT
MRI-CGCM3	MRI, Japan	1.0° × 0.5°	SIC,SND,SIT
NorESM1-M	NCC, Norway	1.1° × 0.43°	SIC,SND,SIT
NorESM1-ME	NCC, Norway	1.1° × 0.43°	SIC,SND,SIT
BCC-CSM1-1	BCC, China	1.0° × 0.82°	SIC,SND,SIT
BCC-CSM1-1-m	BCC, China	1.0° × 0.82°	SIC,SND,SIT
INMCM44	INM, Russia	0.75° × 0.41°	SIC,SND,SIT
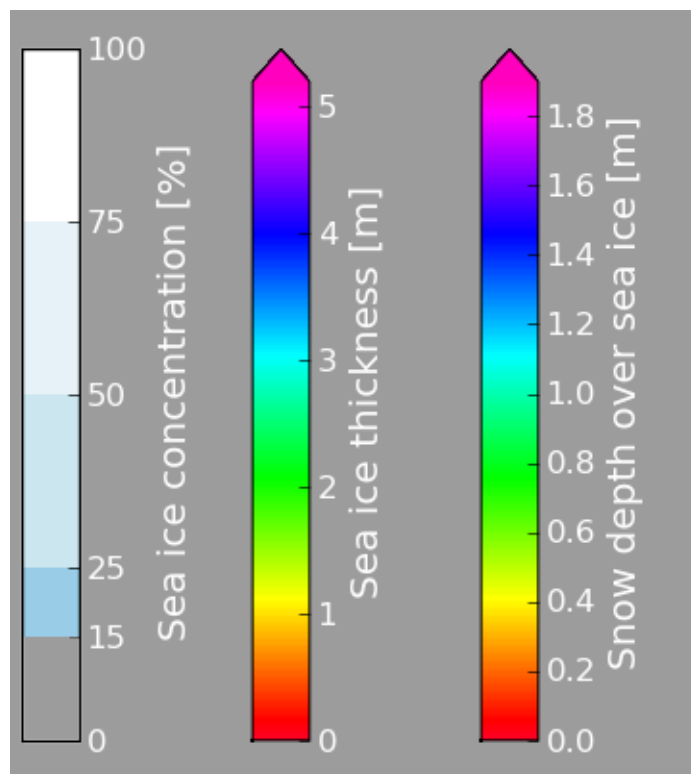
Figure 2.1: Examples of colorbars for sea ice concentration, thickness and snow depth.

contract agreement.

Examples of climatological maps provided in KMZ format are given in figures 2.2, 2.3 and 2.4 for three different models.
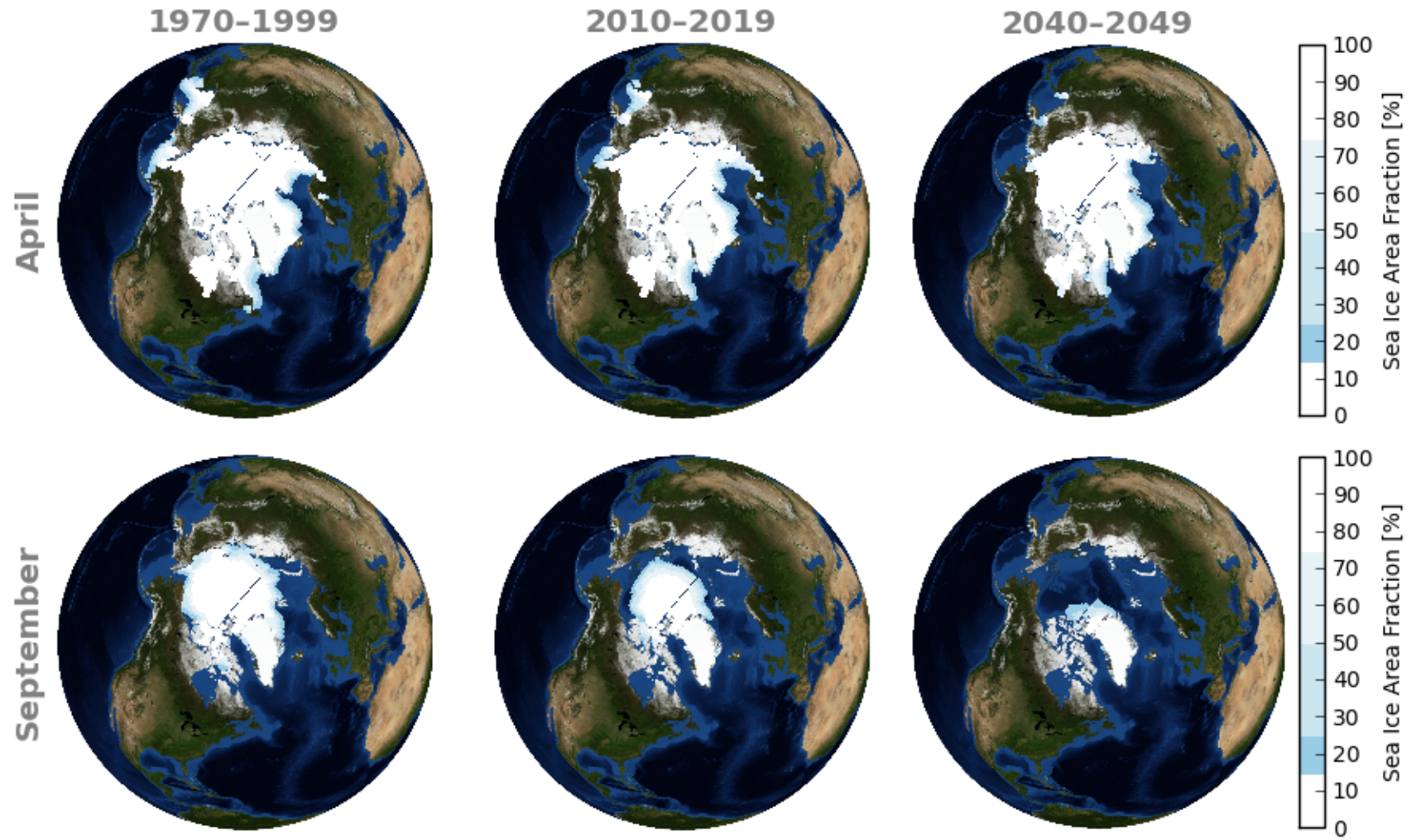
Figure 2.2: Example of monthly sea ice concentration climatologies from the GFDL-CM3 model for the months of September and April over the historical period, the 2010–2020 and 2040–2050 decades.

Figure 2.3: Example of monthly sea ice thickness climatologies from the MIROC5 model for the months of September and April over the historical period, the 2010–2020 and 2040–2050 decades.

Figure 2.4: Example of monthly snow depth climatologies from the MPI-ESM-MR model for the months of September and April over the historical period, the 2010–2020 and 2040–2050 decades.

2.3   Ice free days gradient lines

To illustrate the pattern of sea ice retreat, we are comput-
ing ice free days contour lines. These isolines connect grid
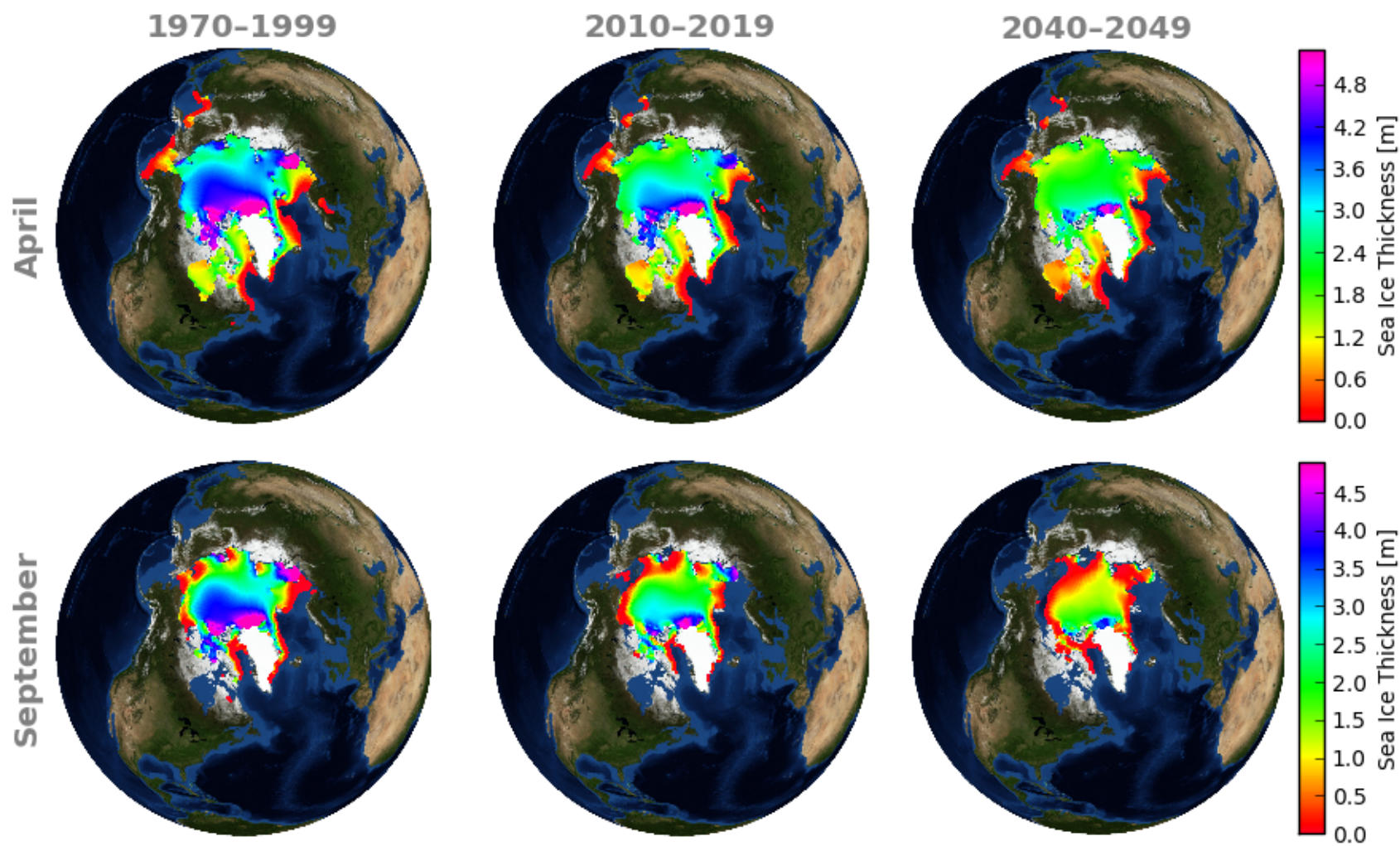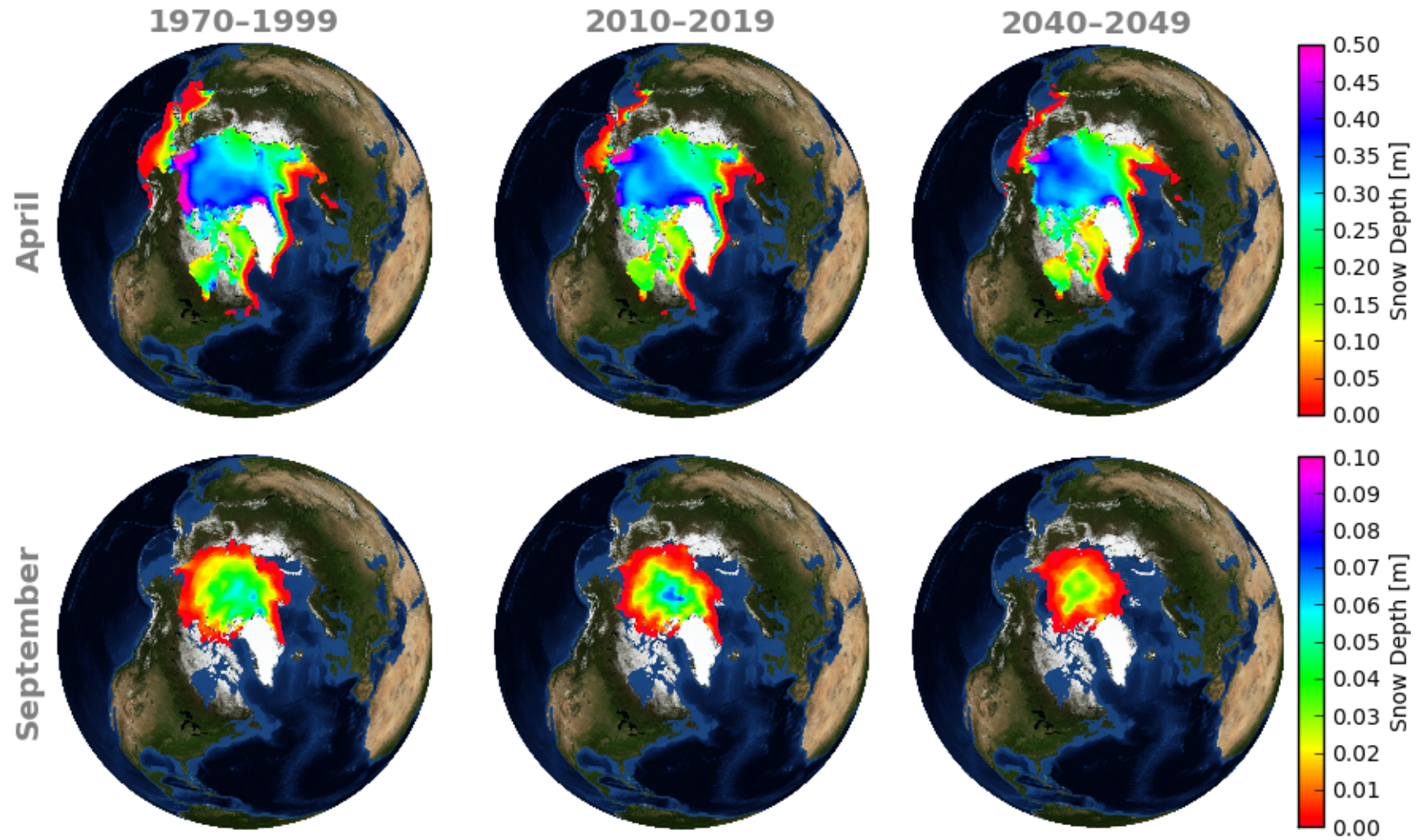cells that have the same number of ice free days per year on
average. Isolines are computed for each averaging period,
that is 1970–1999 for the Historical experiment and individ-
ual decades from 2010 to 2099 for the RCP experiments. A
grid cell is considered ice free if the average sea ice concen-
tration in a given month is below 15%. For each grid cell,
the number of days during each ice free month are accu-
mulated for all months to yield the number of ice free day
per year. This yields a grid of values representing the av-
erage number of days per year where no ice is present. A
contouring algorithm draws isolines for each increment of
ten ice free days[2]. Each contour line is tagged with a cus-
tom style and color linked to the colormap shown in figure
2.5. So for example, regions enclosed between blue lines are
those that are ice covered for most of the year, while regions
within orange or red lines remain ice free most of the year.
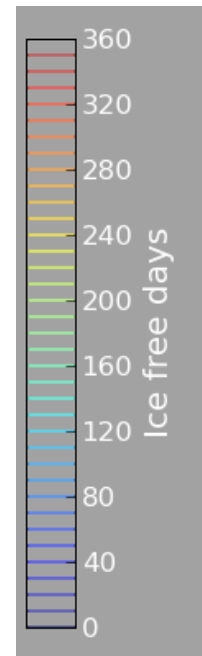An example is shown in figure 2.6.

Figure 2.5:   Colormap
for ice free days isolines.

2.4   CCSM4 ice thickness categories

We use the ice thickness category diagnostics as a proxy for
ice age. Indeed, ice age is a variable that is not routinely computed or archived by
climate models. On the other hand, the thickness and shape of sea ice are closely
linked to its age. Newly formed ice is thin and level, but as winds and currents drive
ice floes against one other, ridges and hummocks form. As the ice ages, some of its
properties change, such as compressive strength and salinity. To take these vari-
ations into account, many ice models implement ice thickness categories, meaning
that ice of different thicknesses are modelled independently. Concentrations of thick
ice can be interpreted as concentrations of old ice, while concentrations of thin ice
can be interpreted as concentrations of newly formed ice. While the relationship is
not perfect, it is thought to hold well enough to be useful.

CMIP5 experimental guidelines require modelling teams to submit bulk sea ice
concentration values. Sea ice concentrations by ice thickness category are not di-
rectly available through the CMIP5 archive. The CCSM4 model however stores these
values for internal analysis and distributes them through the ESG National Center
for Atmospheric Research (NCAR) gateway. CCSM4 defines five ice categories (m): [0,
.64], [.64, 1.39], [1.39, 2.47], [2.47, 4.57] and [4.57, ∞]. The CCSM4 sea ice thickness di-
agnostics are post-processed in the same manner as for the sea ice concentration of

---

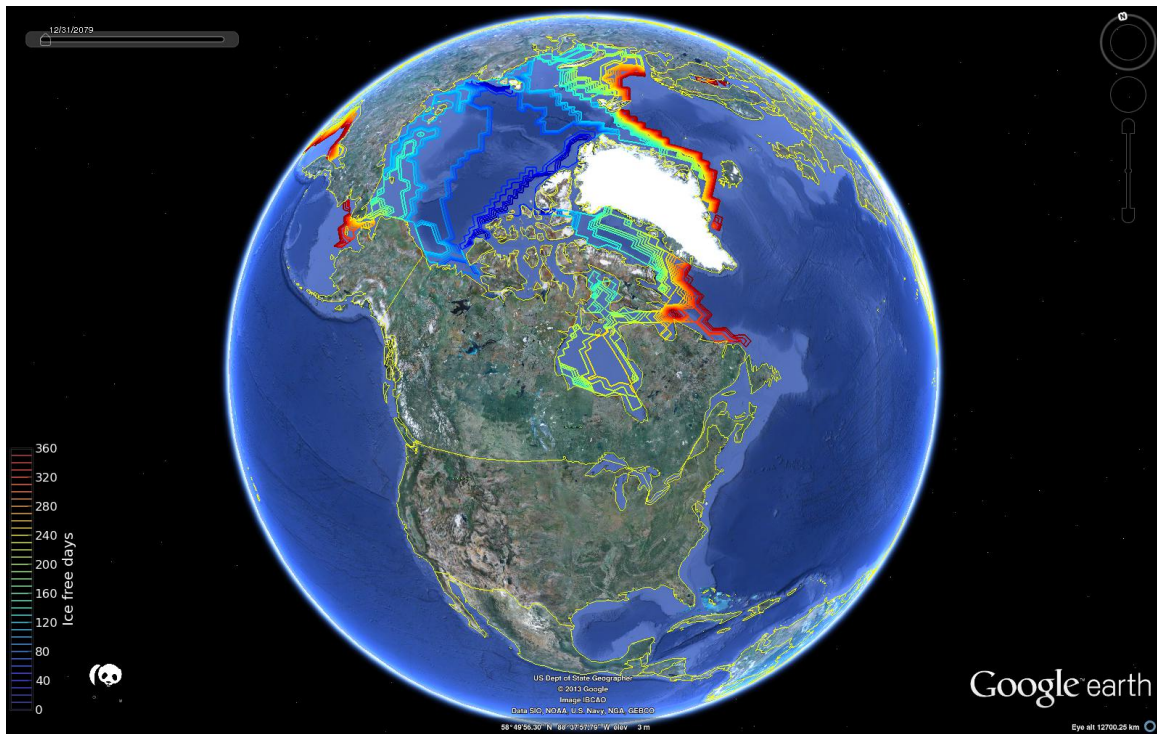[2]These lines are saved in vector format in a KLM file as `<LineStrings>`.

Figure 2.6: Ice free days isolines for model IPSL-CM5A-MR driving by RCP8.5 over decade 2080–2090.

the CMIP5 data. Note that the colormap is transparent where *bulk* ice concentrations are below 15%.

Part B: High resolution simulation of Arctic sea ice

While the large GCM ensemble allows for an appraisal of sea ice loss in the Arctic Ocean, GCM resolution is insufficient to resolve the intricate channels of the Canadian Arctic Archipelago (CAA). One solution is to downscale GCM results at a finer scale using a regional model. While climate simulations at finer scale require more computing resources, the higher resolution is offset by restricting computations to a smaller domain. In the following, we use the MITgcm in regional mode to downscale the results of one GCM unto a high-resolution Arctic grid.

3.1   MITgcm

The MITgcm is a versatile model that can be used to study the atmosphere, the ocean, sea ice or combinations of the above [*Adcroft et al.*, 2012]. It can be applied at multiple scales, from global simulations to laboratory tank experiments.

For the purpose of this study, the MITgcm is used to simulate the ice and ocean over a domain covering the Arctic ocean (see figure 3.1). In this regional configuration, the MITgcm requires boundary conditions and atmospheric forcing fields. Boundary conditions specify ocean velocity, salinity and temperature on each side of the model domain. Seven atmospheric forcing fields must be prescribed to drive the coupled ice-ocean model: eastward and northward surface wind velocity, surface air temperature, specific humidity, precipitation, solar radiation, downward long-wave radiation and river runoff if available.

Boundary conditions, model parameters and bathymetry have been generously provided by MIT research scientist An T. Nguyen. *Nguyen et al.* [2011] optimized the parameters to reproduce correctly observed sea ice concentrations, fluxes and thicknesses when the MITgcm is driven by atmospheric fields from the Japanese 25-year Reanalysis Project (JRA-25) [*Onogi et al.*, 2007]. In this configuration, the model has an horizontal resolution of 18km.
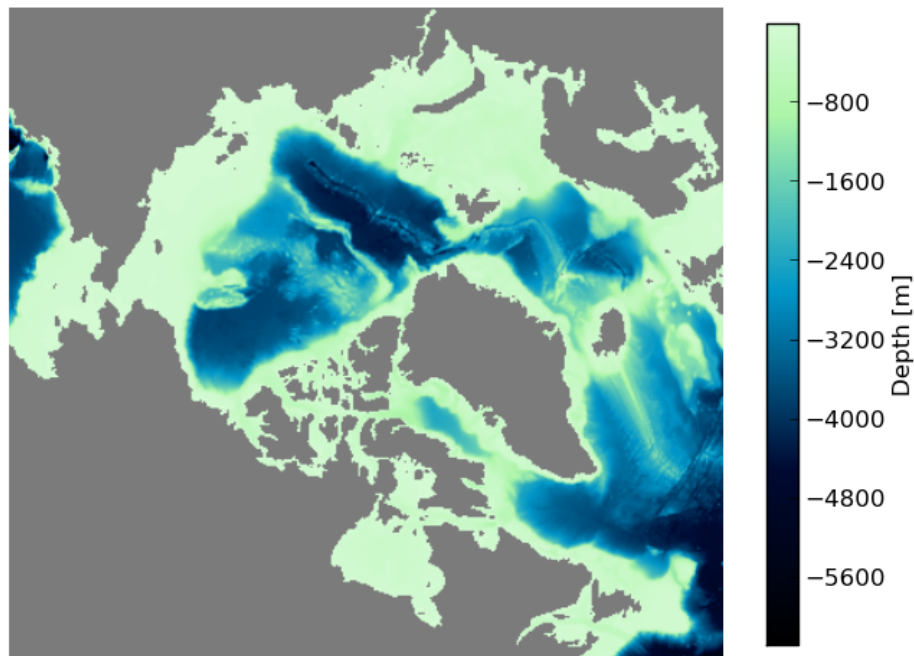
Figure 3.1: Bathymetry of the MITgcm Arctic domain.

3.2   MITgcm **drivers**

For the purpose of this work, the MITgcm is run using two different atmospheric forc-
ing fields. To validate the model behavior, the MITgcm is first run using JRA-25 atmo-
spheric forcing fields at a 6-hourly resolution. This run starts in January 1992 and
ends in December 2005. The model is then run using forcing fields from the GFDL
Climate Model version 3 (GFDL-CM3) at a 3-hourly resolution from January 2006 to
December 2079.

    The GFDL-CM3 model was selected to drive the MITgcm since among models that
have been analyzed in part A, it stands out as a model whose ice concentration over
the historical period displays a realistic spatial distribution and thickness. Also, data
at high temporal frequency (3h) was readily available on a regular grid, simplifying
its integration as external forcing to the MITgcm. Finally, we are working jointly with
colleagues at the Jet Propulsion Laboratory (JPL) who have close collaboration with
developers at the Geophysical Fluid Dynamics Laboratory (GFDL).

3.3 Boundary conditions

Ocean temperature, salinity and velocity must be prescribed at the domain boundaries. For the JRA-25 run, these lateral boundary conditions are derived from a global simulation generated by the Estimating the Circulation and Climate of the Ocean, Phase II (ECCO2) project [*Menemenlis et al.*, 2008]. Since this simulation did not extend in the future, we have no lateral boundary conditions for the run spanning the 2012–2080 period. For GFDL-CM3 driven simulation, we randomly selected years from the period 1990–2011 to create synthetic boundary conditions from 2012 to 2080. The effect of the lateral boundary conditions will be studied in a subsequent simulation — see contract extension for details.

3.4 Atmospheric forcing fields

The MITgcm has been shown to reproduce well observed sea ice conditions when driven by JRA-25 atmospheric forcing fields [*Nguyen et al.*, 2011]. The question is whether the model will perform similarly well when driven by GFDL-CM3. Different models make different trade-offs in the complexity and realism of the myriad climate processes. This is especially true for surface variables that are influenced by the land surface details of each model. There is thus no guarantee that the MITgcm will perform well when driven by another forcing data set.

Figures 3.2 to 3.5 present the annual mean of the seven forcing variables driving the MITgcm for JRA-25 and GFDL-CM3. The bottom row shows the differences between the two averages. GFDL-CM3 appears to be slightly colder than JRA-25 over the Arctic ocean. The largest differences however occur for the short- and long-wave downward radiation fields. Compared to JRA-25, GFDL-CM3 underestimates solar radiation and overestimates longwave radiation.

3.5 Bias correction factors

The comparison of mean fields from JRA-25 and GFDL-CM3 shows differences that are not due to random fluctuations. These differences are called biases and it is good practice to remove those biases before driving an impact model. This is especially relevant in this case since the parameters of the MITgcm have been selected to reproduce observations correctly when driven by JRA-25. Figures 3.6 to 3.11 illustrate the differences in monthly averages between JRA-25 and GFDL-CM3. Bottom panels display both the additive bias and the multiplicative factor that describe the difference between the two values.

The strategy followed here is to compute for each forcing field and each month an average correction, either additive or multiplicative, that is applied to the 3-hourly GFDL-CM3 forcing fields. These corrections are computed over the period 2005–2011 and presented in table 3.1. The period 2005–2011 is considerably shorter than the 30 years typically used to compute normals, thus the computed biases are bound to
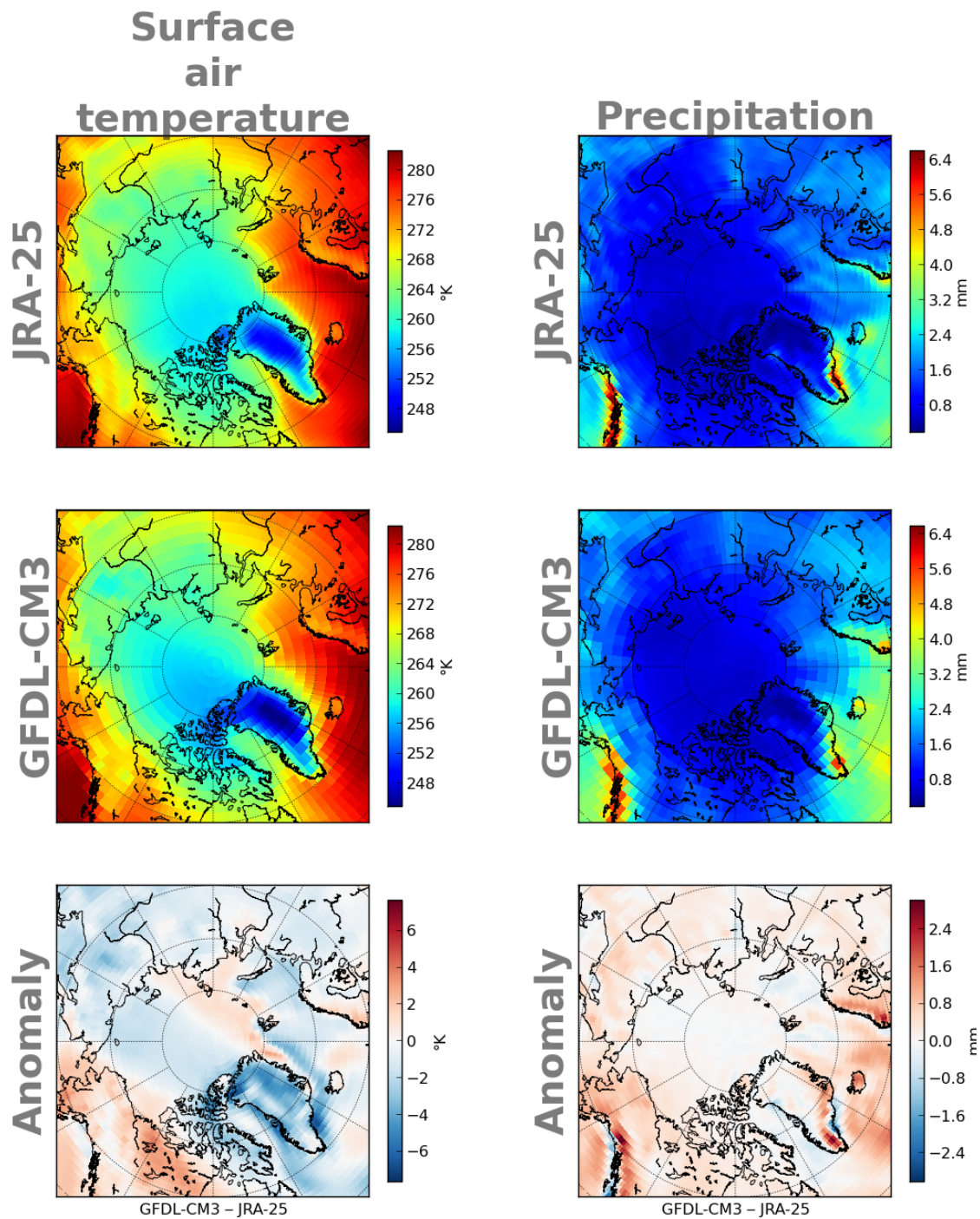
Figure 3.2: Difference in mean temperature and precipitation between JRA-25 and GFDL-CM3 during the period 2005–2011.
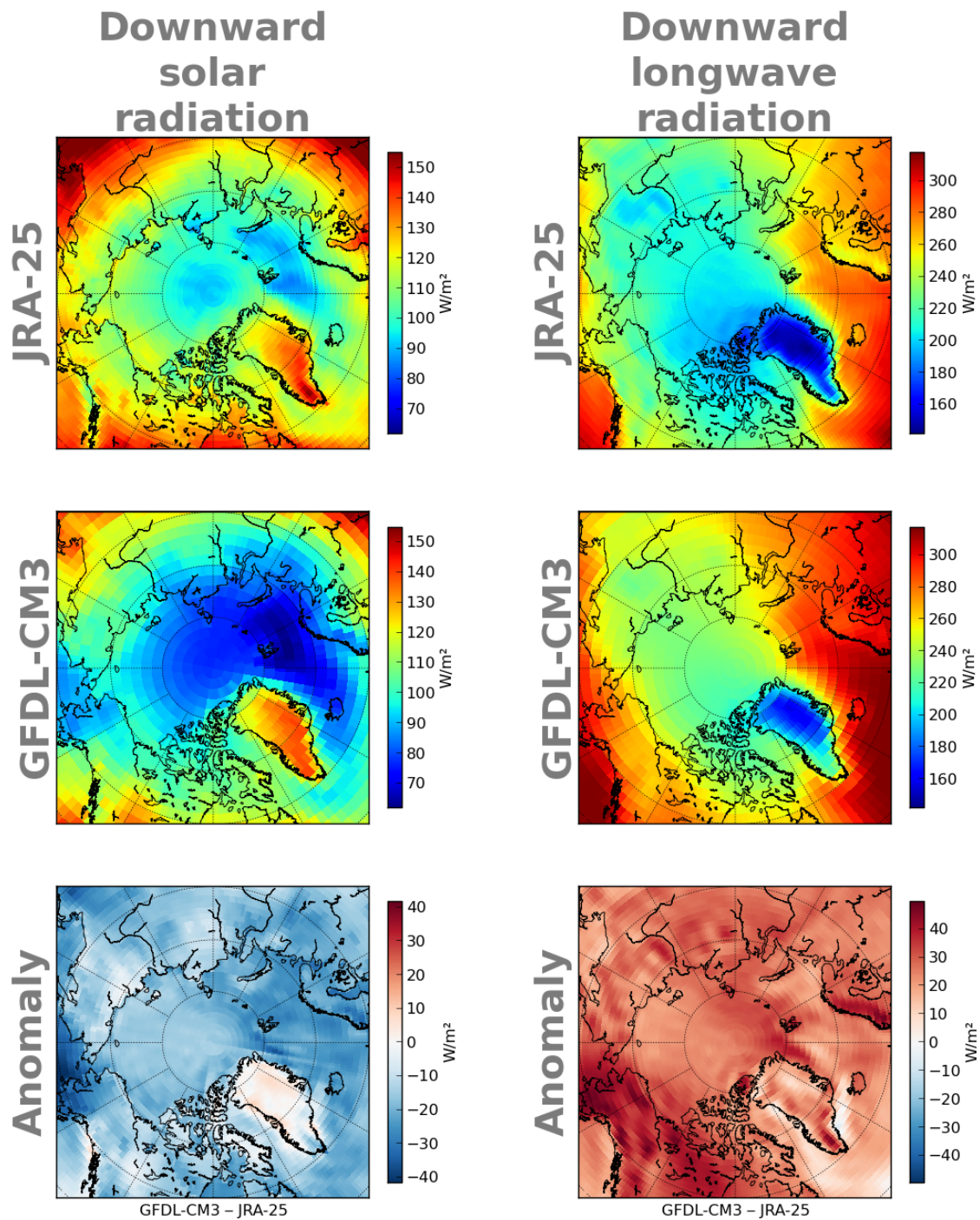
Figure 3.3: Difference in mean solar and longwave downward radiation between JRA-25 and GFDL-CM3 during the period 2005–2011.
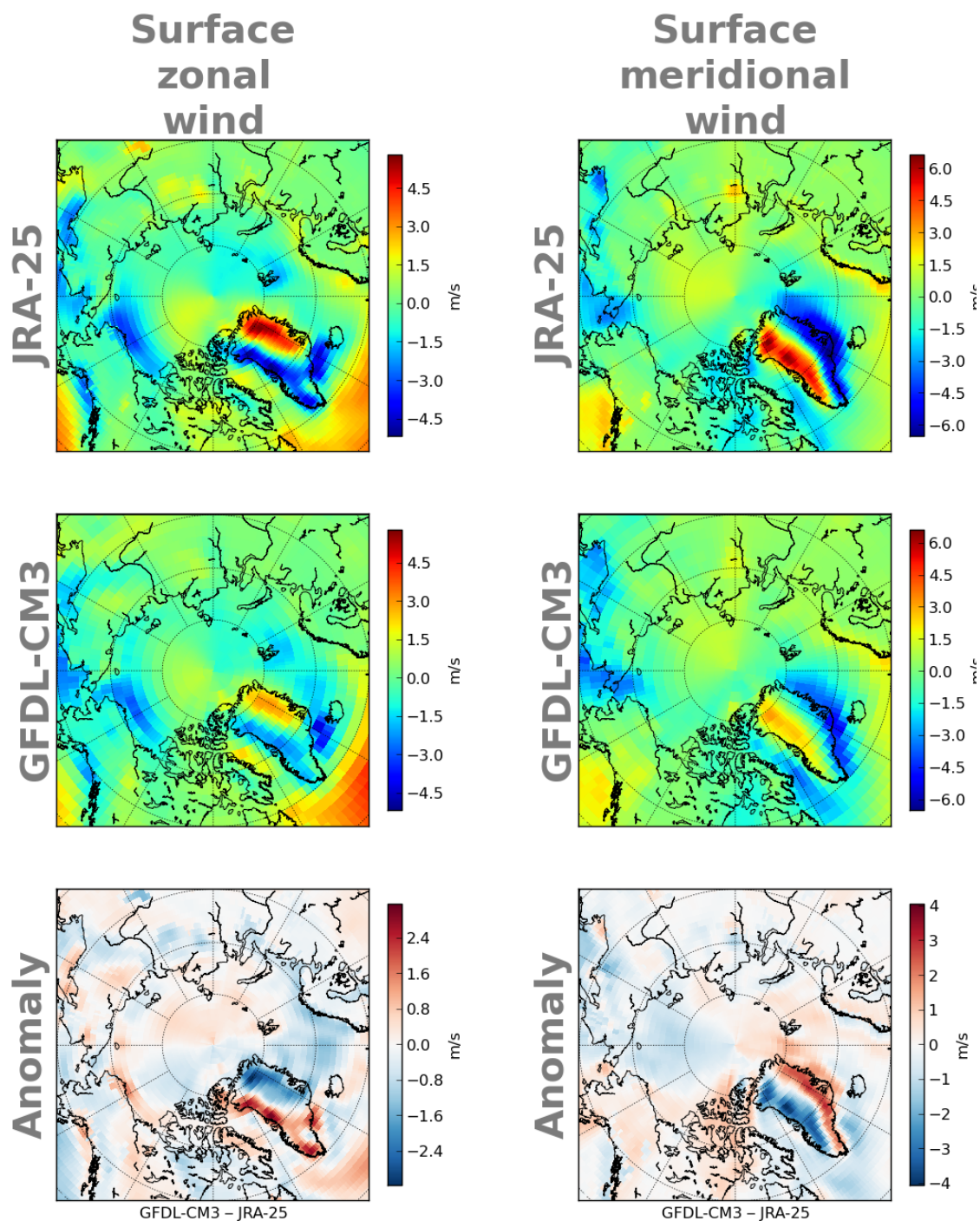
Figure 3.4: Difference in mean eastward and northern surface wind speed between JRA-25 and GFDL-CM3 during the period 2005–2011.
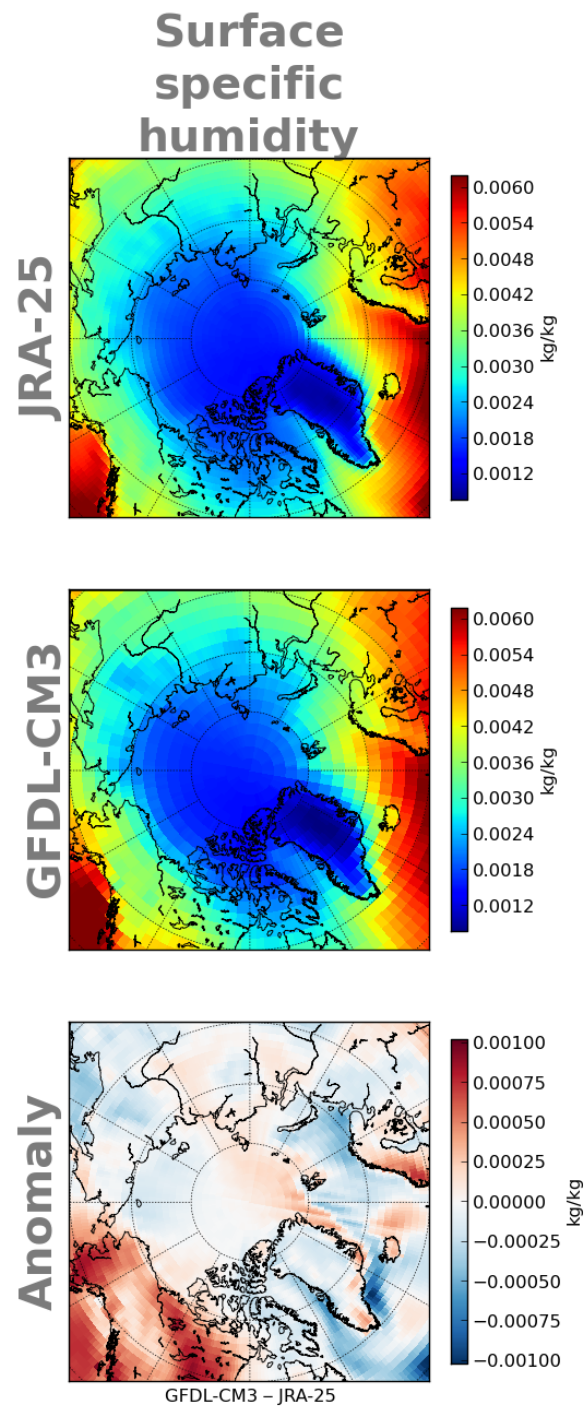
Figure 3.5: Difference in mean specific humidity between JRA-25 and GFDL-CM3 during the period 2005–2011.
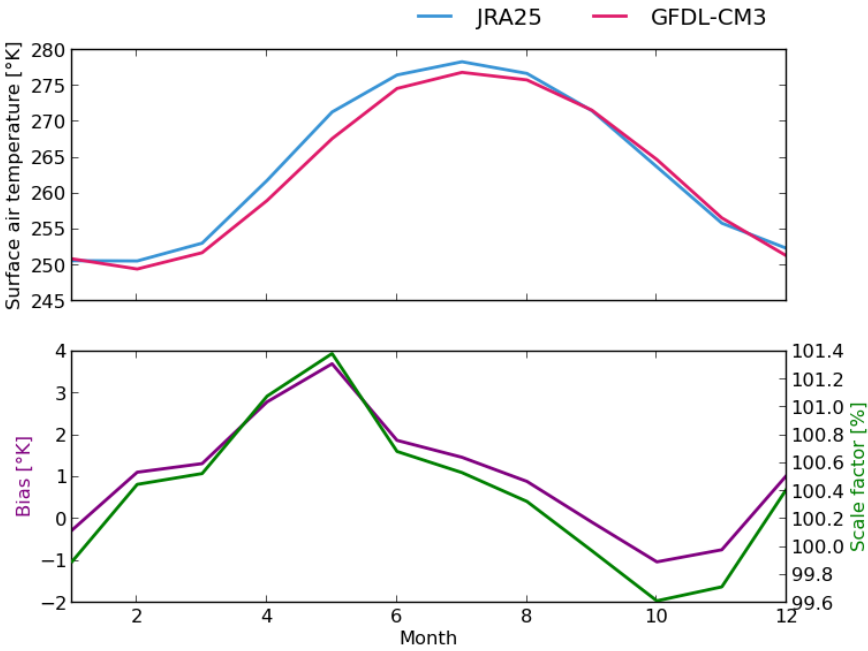
Figure 3.6: Monthly averages computed over the Arctic for the JRA-25 and GFDL-CM3 surface temperature. The bottom panel shows their difference (JRA-25 − GFDL-CM3) and ratios (JRA-25/GFDL-CM3).
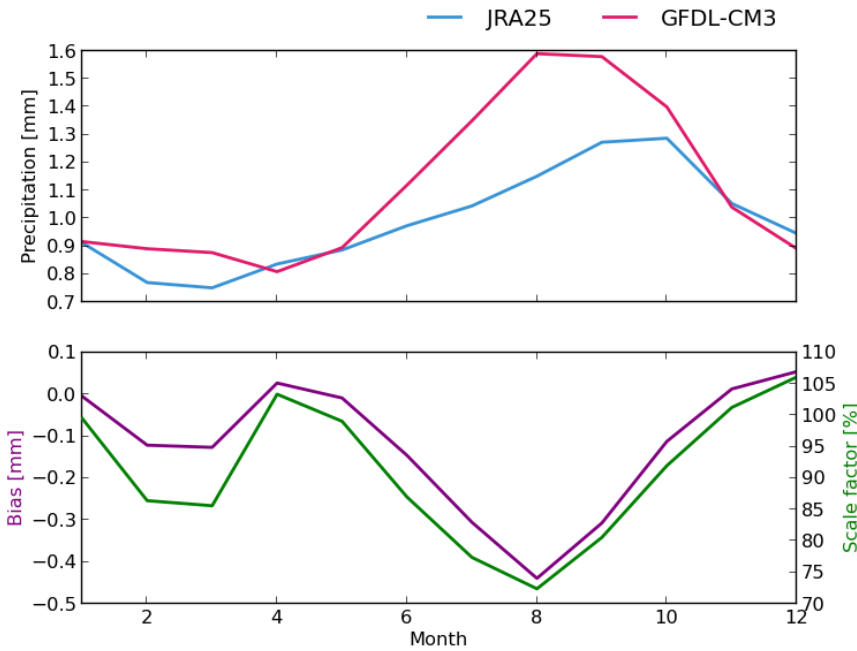

Figure 3.7: Monthly averages computed over the Arctic for the JRA-25 and GFDL-CM3 precipitation. The bottom panel shows their difference (JRA-25 − GFDL-CM3) and ratios (JRA-25/GFDL-CM3).
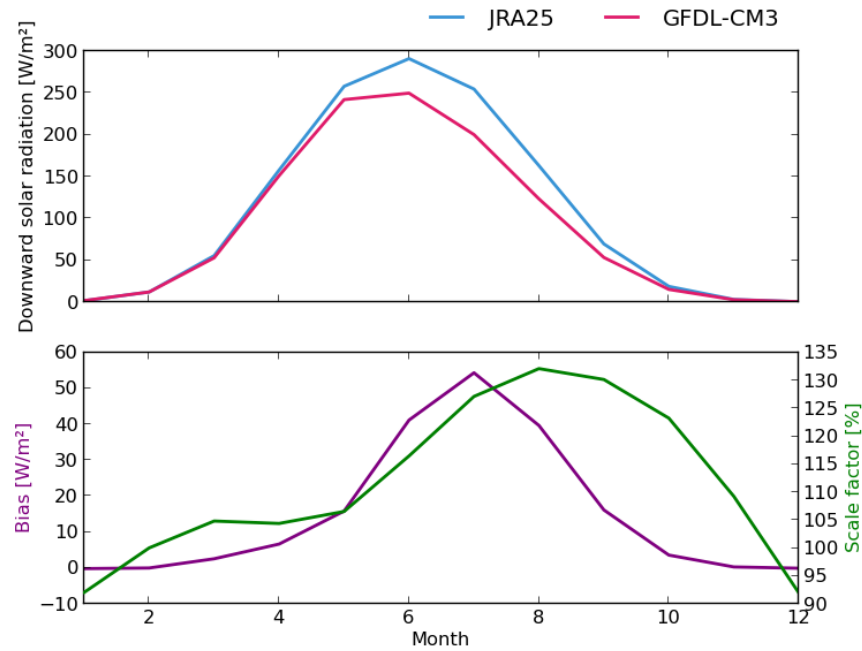
Figure 3.8: Monthly averages computed over the Arctic for the JRA-25 and GFDL-CM3 solar radiation. The bottom panel shows their difference (JRA-25 − GFDL-CM3) and ratios (JRA-25/GFDL-CM3).

Figure 3.9: Monthly averages computed over the Arctic for the JRA-25 and GFDL-CM3 downward longwave radiation. The bottom panel shows their difference (JRA-25 − GFDL-CM3) and ratios (JRA-25/GFDL-CM3).

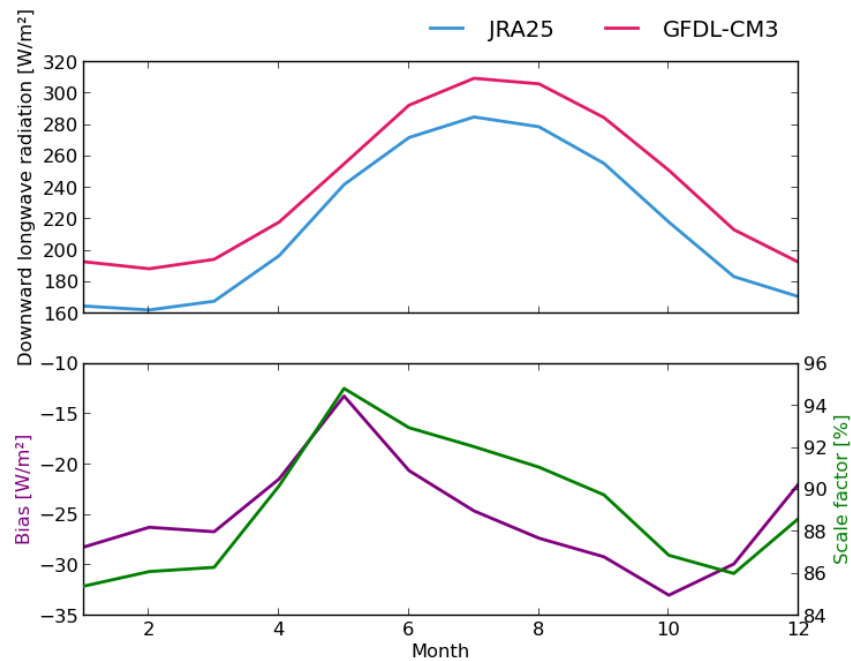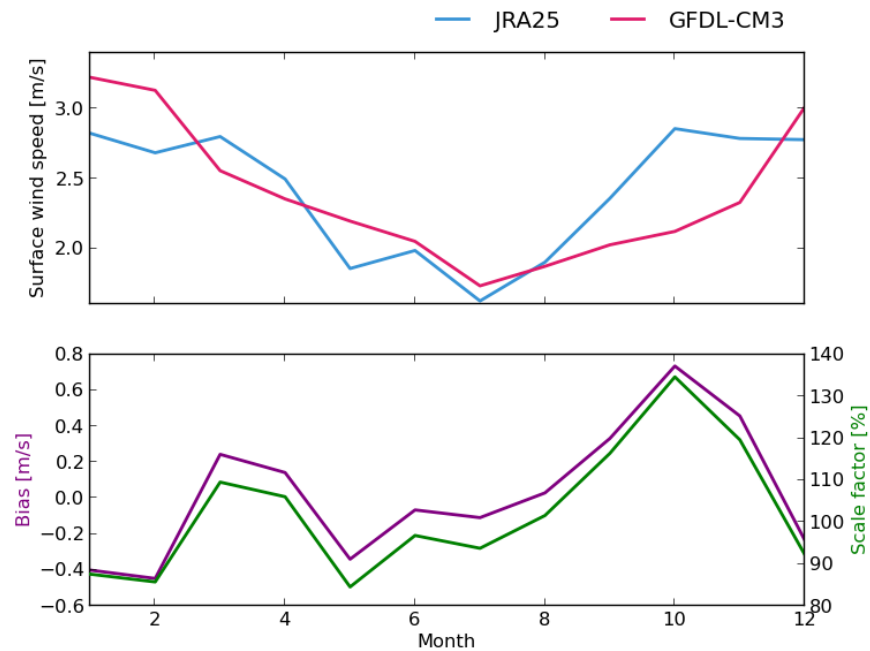Figure 3.10: Monthly averages computed over the Arctic for the JRA-25 and GFDL-CM3 surface wind velocity. The bottom panel shows their difference (JRA-25 − GFDL-CM3) and ratios (JRA-25/GFDL-CM3).
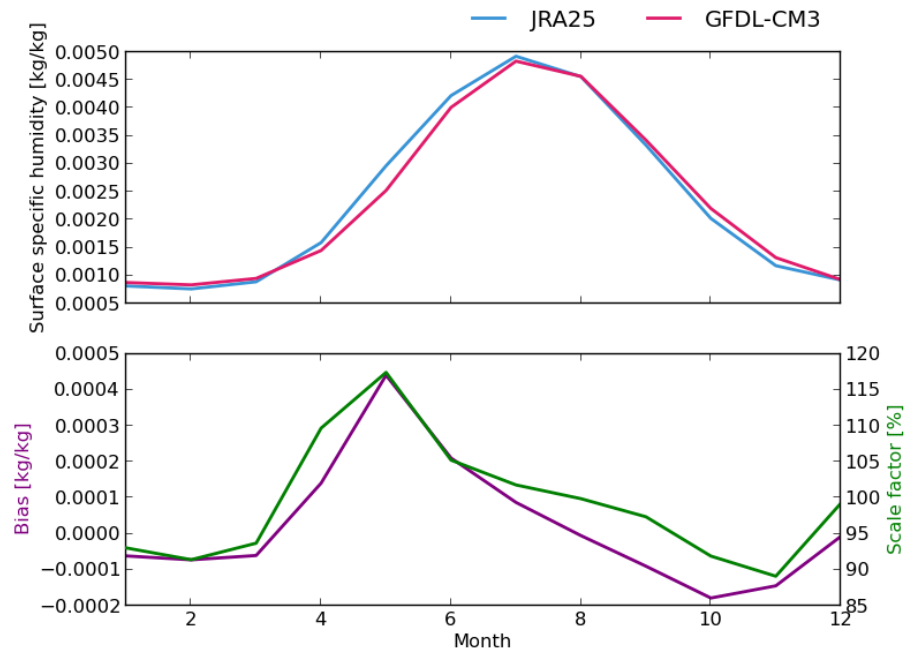
Figure 3.11: Monthly averages computed over the Arctic for the JRA-25 and GFDL-CM3 surface specific humidity. The bottom panel shows their difference (JRA-25 − GFDL-CM3) and ratios (JRA-25/GFDL-CM3).

be influenced by natural variability [*Hawkins and Sutton*, 2009]. The decision to use a shorter time scale is motivated by trying to smooth the transition from the end of the JRA-25 simulation and the beginning of the GFDL-CM3 simulation, considering that there are trends in the Arctic climate since the last few decades. The effect of using biases computed on a longer time frame will be evaluated in future work.

Table 3.1: Biases applied to the GFDL-CM3 forcing fields. Biases are applied additively where units are given, otherwise they are multiplicative factors.

	Surface air temperature	Precipitation	Surface specific humidity	Downward solar radiation	Downward longwave radiation	Surface zonal wind
	°K		kg/kg		W/m²	
January	0.54	0.96	-3.9e-05	0.97	-25	1
February	0.92	0.82	-9.3e-05	1	-28	1
March	0.73	0.82	-0.00012	1.1	-29	0.91
April	1.9	0.9	2.1e-05	1.1	-26	1.1
May	2.6	0.95	0.0003	1.1	-19	0.81
June	1.9	0.85	0.00018	1.2	-21	1.1
July	1.5	0.74	6.2e-05	1.3	-25	0.85
August	0.72	0.7	-7.6e-05	1.3	-28	1.2
September	-0.51	0.8	-0.00021	1.3	-31	1.3
October	-1.5	0.98	-0.00025	1.2	-35	1.4
November	-1.5	0.97	-0.00022	1.1	-34	1.3
December	-0.23	0.97	-8.5e-05	0.93	-28	0.92

3.6 Results and validation

The MITgcm outputs user-selected diagnostic fields. For this project, six sea ice variables are archived: fractional ice covered area (SIarea), effective ice thickness (SIheff), effective snow thickness (SIhsnow), effective salinity (SIhsalt), zonal ice velocity (SIuice) and meridional ice velocity (SIvice). Grid information is also included, namely grid cell area (rA) and grid cell centers in geographical coordinates (XC, YC).[1]

Figures 3.12 and 3.13 show monthly time series of sea ice extent and volume. The JRA-25 driven simulation tracks well observed quantities and the transition from JRA-25 to GFDL-CM3 is imperceptible. Minimum September sea ice extent observations were obtained from NSIDC while the monthly time observations are estimated from brightness temperature data derived from Nimbus-7 Scanning Multichannel Microwave Radiometer (SMMR) and Defense Meteorological Satellite Program Special Sensor Microwave/Imager (SSM/I) [*Cavalieri et al.*, 1996, updated 2008]. Sea ice volume observations are taken from Pan-Arctic Ice Ocean Modeling and Assimilation System (PIOMAS) [*Zhang and Rothrock*, 2003].

September sea ice vanishes completely over the period 2045–2055, and although the maximum extent does not decrease as rapidly as the minimum extent, it is clear by the volume time series that the ice volume has a decreasing trend. Results indicate we should expect multi-year ice to disappear completely during the next 50 years.

Figures 3.14 and 3.15 display maps of mean sea ice concentration and effective ice thickness averaged over all months of September over the periods 2010–2019 and 2040–2049 respectively. These figures show clearly that the last remnants of ice collect along Queen Elisabeth Islands, and that the NorthWest Passage inside the CAA is completely ice-free. Note that numerical artifacts near the pole are visible in figure 3.14. This is likely due to an interpolation issue going from the GFDL-CM3 regular grid to the MITgcm curvilinear grid and will be investigated in more details.

---

[1]Two netCDF files storing these fields have been made available to WWF at `meteo.mcgill.ca/ ~huardda/wwf`.
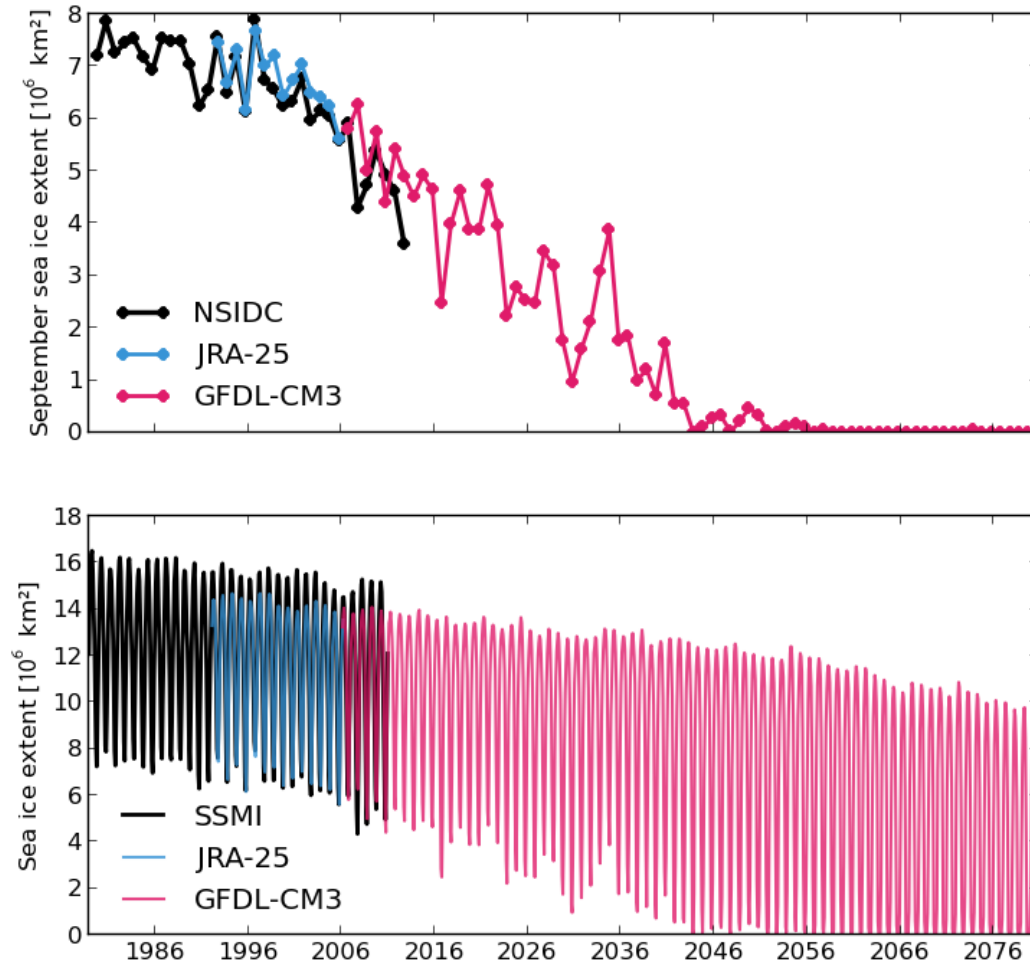
Figure 3.12: Sea ice extent time series. The top panel shows September sea ice extent and the bottom panel the monthly time series.
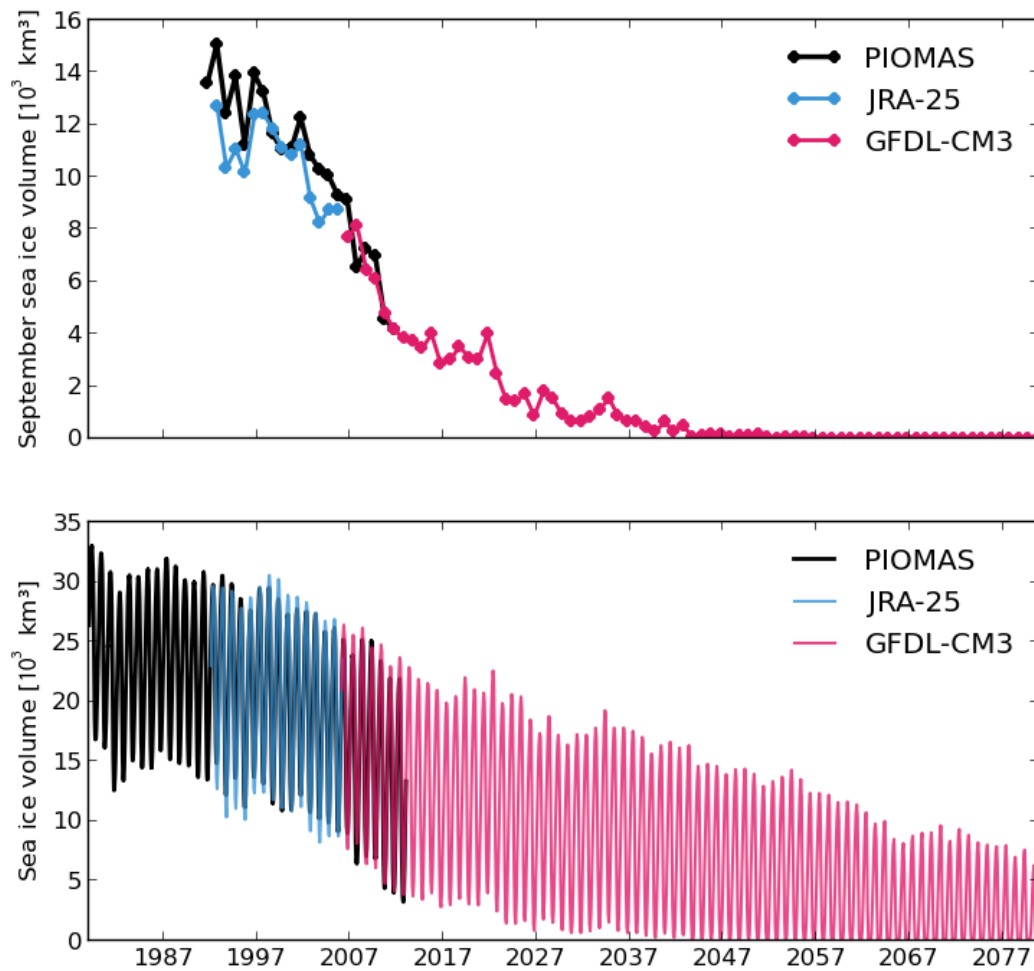
Figure 3.13: Sea ice volume time series. The top panel shows September sea ice volume and the bottom panel the monthly time series.
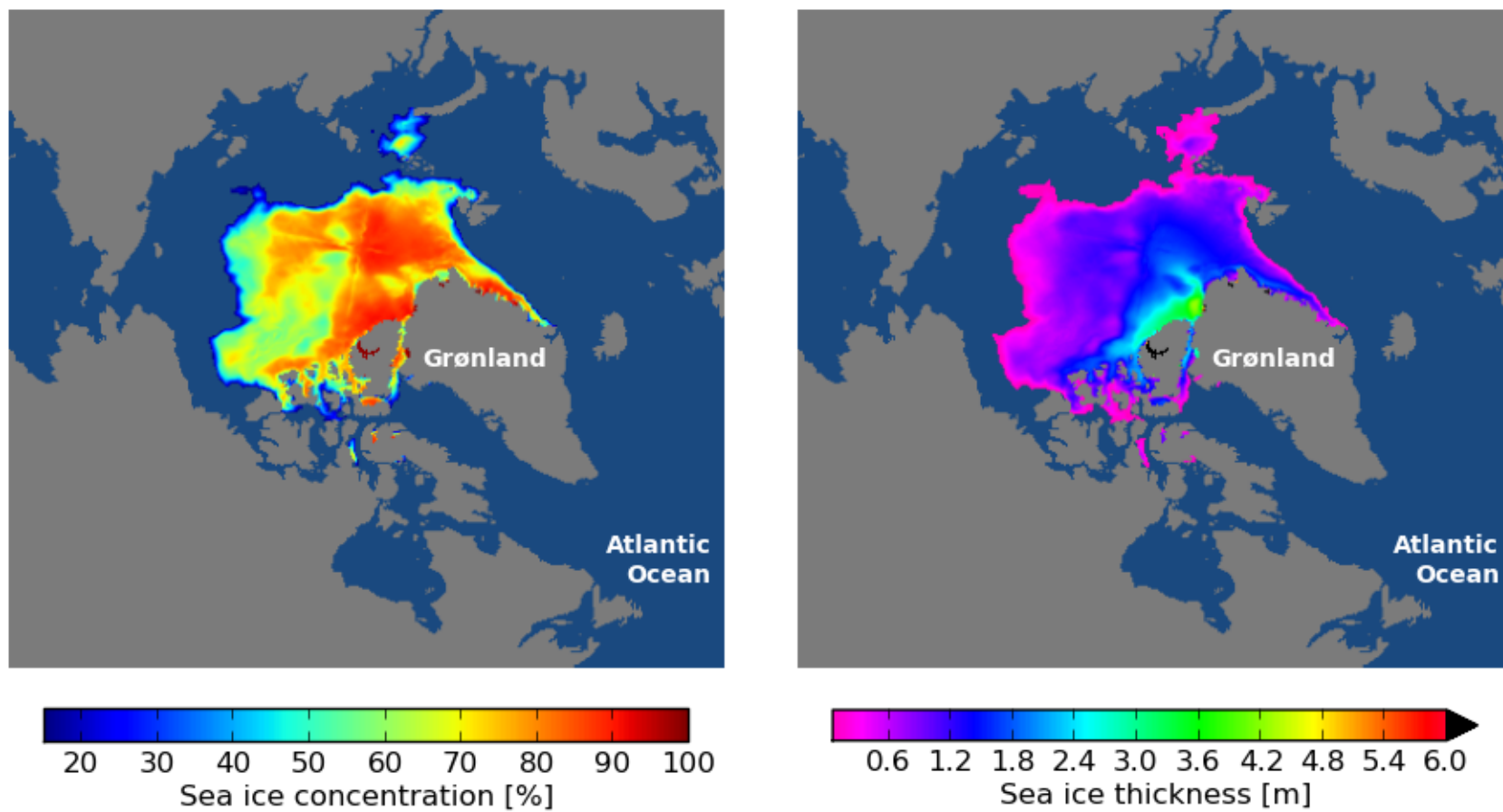
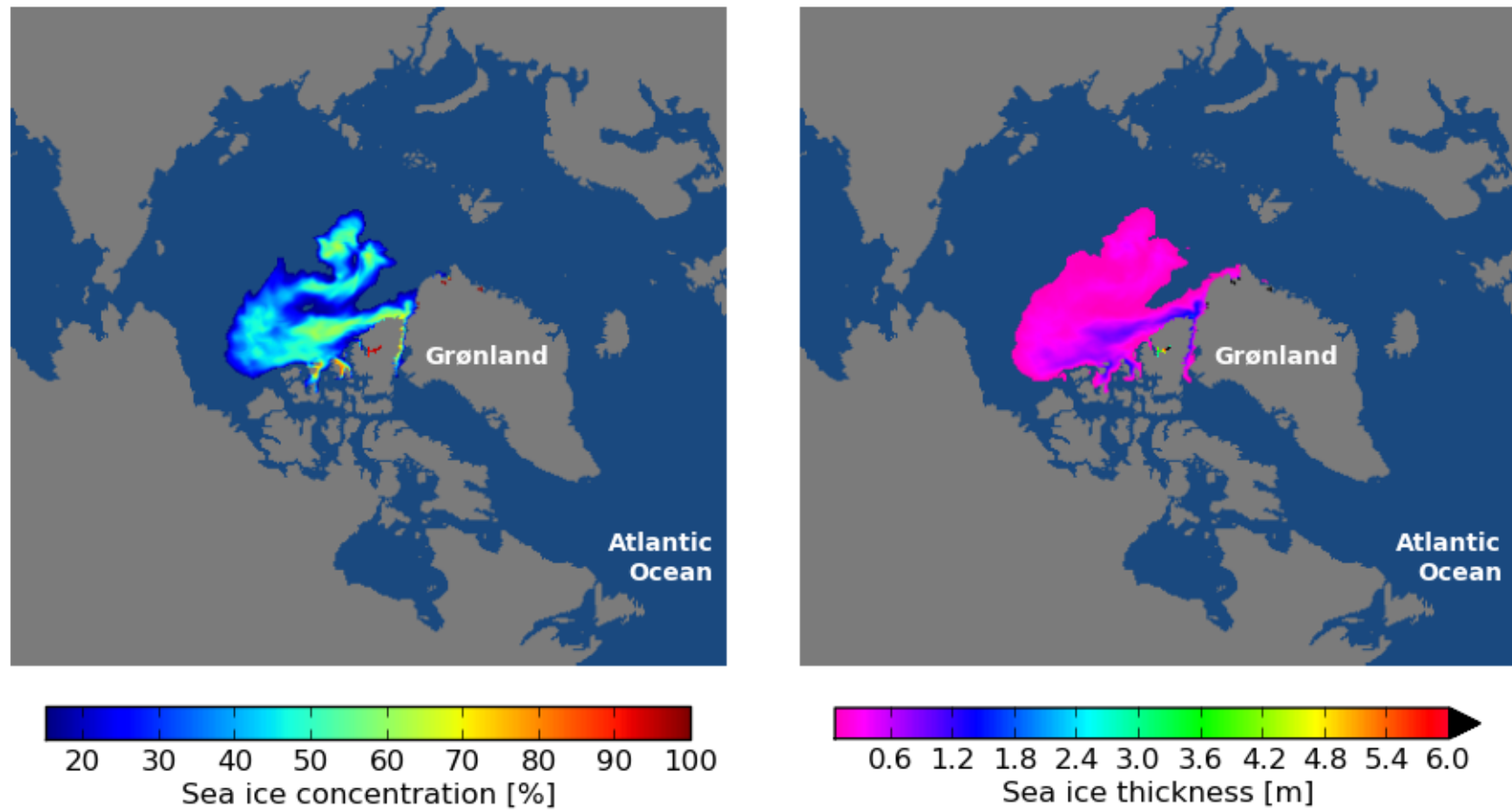Figure 3.14: September sea ice concentration (left) and thickness (right) over the decade 2010-2020.

Figure 3.15: September sea ice concentration (left) and thickness (right) over the decade 2040-2050.

3.7 Conclusion

This work has analyzed an ensemble of CMIP5 participating GCMs to document projected Arctic sea ice retreat. Climatological averages of sea ice concentration, thickness and snow depth were computed for the historical period and two future scenarios going from 2006 to 2100. Ice free days gradients were computed in each case to display the patterns of sea ice retreat. An additional analysis focused on ice concentrations according to its thickness was performed with CCSM4 projections to study the fate of multi-year ice.

In the second part of this work, the MITgcm was used to simulate sea ice conditions in the Arctic from 1992 to 2080. The coupled ocean and ice model was driven by atmospheric forcing from JRA-25 reanalyses from 1992 to 2006 and with a climate projection from GFDL-CM3 from 2006 to 2080. Results agree well with sea ice extent and volume observations over the historical period. Sea ice projections indicate a complete disapearance of September sea ice around 2050. Additional runs will be performed to investigate the effect of lateral boundary conditions and bias corrections on the results.

Acknowledgements

Acronyms

AORI Atmosphere and Ocean Research Institute

BCC Beijing Climate Center

BNU Beijing Normal University

BOM Bureau of Meteorology

CAA Canadian Arctic Archipelago

CCCma Canadian Centre for Climate Modelling and Analysis

CCSM4 Community Climate System Model version 4

CMIP5 Coupled Model Intercomparison Project phase 5

CMCC Centro Euro-Mediterraneo per I Cambiamenti Climatici

CNRM-CERFACS Centre National de Recherches Météorologiques / Centre Européen de Recherche et Formation Avancées en Calcul Scientifique

CO$_2$ carbon dioxide

CSIRO Commonwealth Scientific and Industrial Research Organisation

DOE Department of Energy

ECCO2 Estimating the Circulation and Climate of the Ocean, Phase II

ESG Earth System Grid

GCESS College of Global Change and Earth System Science

GCM Global Coupled Model

GFDL Geophysical Fluid Dynamics Laboratory

GFDL-CM3 GFDL Climate Model version 3

GHG greenhouse gases

GHGA greenhouse gases and aerosols

GISS Goddard Institute for Space Studies

INM Institute for Numerical Mathematics

IPSL Institut Pierre-Simon Laplace

JAMSTEC Japan Agency for Marine-Earth Science and Technology

JPL Jet Propulsion Laboratory

JRA-25 Japanese 25-year Reanalysis Project

LASG-IAP LASG, Institute of Atmospheric Physics, Chinese Academy of Sciences

MITgcm Massachusetts Institute of Technology general circulation model

MOHC Met Office Hadley Centre

MPI-M Max Planck Institute for Meteorology

MRI Meteorological Research Institute

NASA National Aeronautics and Space Administration

NCAR National Center for Atmospheric Research

NCC Norwegian Climate Centre

NIES National Institute for Environmental Studies

NOAA National Oceanic and Atmospheric Administration

NSF National Science Foundation

NSIDC National Snow & Ice Data Center

PIOMAS Pan-Arctic Ice Ocean Modeling and Assimilation System

RCP4.5 Radiative Concentration Pathway 4.5

RCP8.5 Radiative Concentration Pathway 8.5

Bibliography

Adcroft, A., et al., Mitgcm user manual, *Tech. rep.*, MIT Department of Earth, Atmospheric and Planetary Sciences, 2012.

Cavalieri, D., C. Parkinson, P. Gloersen, and H. J. Zwally, Sea ice concentrations from Nimbus-7 SMMR and DMSP SSM/I passive microwave data, *Digital media*, Boulder, Colorado USA: National Snow and Ice Data Center, 1979-2007, 1996, updated 2008.

Deser, C., A. Phillips, V. Bourdette, and H. Teng, Uncertainty in climate change projections: the role of internal variability, *Climate Dynamic*, *38*(3-4), 527–546,, doi: 10.1007/s00382-010-0977-x, 2010.

Forster, P., et al., *Climate Change 2007: The Physical Science Basis. Contribution of Working Group I to the Fourth Assessment Report of the Intergovernmental Panel on Climate Change*, chap. Changes in Atmospheric Constituents and in Radiative Forcing, Cambridge University Press, Cambridge, U.K., 2007.

Hawkins, E., and R. Sutton, The potential to narrow uncertainty in regional climate predictions, *Bulletin of the American Meteorological Society*, *90*(8), 1095–1107, doi: 10.1175/2009BAMS2607.1, 2009.

Held, I. M., and B. J. Soden, Water vapor feedback and global warming, *Annual Review of Energy and the Environment*, *25*(1), 441–475, doi:10.1146/annurev.energy. 25.1.441, 2000.

Menemenlis, D., J. Campin, P. Heimbach, C. Hill, T. Lee, A. Nguyen, M. Schodlock, and H. Zhang, ECCO2: High resolution global ocean and sea ice data synthesis, *Mercator Ocean Quarterly Newsletter*, *31*, 13–21, 2008.

Moss, R. H., et al., The next generation of scenarios for climate change research and assessment, *Nature*, *463*(7282), 747–756, doi:10.1038/nature08823, 2010.

Nguyen, A. T., D. Menemenlis, and R. Kwok, Arctic ice-ocean simulation with optimized model parameters: Approach and assessment, *Journal of Geophysical Research: Oceans*, *116*(C4), C04025, doi:10.1029/2010JC006573, 2011.

Onogi, K., et al., The jra-25 reanalysis, *Journal of the Meteorological Society of Japan. Ser. II*, *85*(3), 369–432, 2007.

Taylor, K. E., R. J. Stouffer, and G. A. Meehl, An Overview of CMIP5 and the Experiment Design, *Bull. Amer. Meteor. Soc.*, *93*(4), 485–498, 2011.

Zhang, J., and D. Rothrock, Modeling global sea ice with a thickness and enthalpy distribution model in generalized curvilinear coordinates, *Monthly weather review*, *131*(5), 845–861, 2003.